ARTICLES

Pair distribution function and x-ray absorption signatures of rotational and radial local distortions in a model system with average long-range order

D. A. Dimitrov, A. L. Ankudinov, A. R. Bishop, and S. D. Conradson
Los Alamos National Laboratory, Los Alamos, New Mexico 87545
(Received 2 April 1998)

The signatures of local distortions in three-dimensional crystalline structures are studied by calculating extended x-ray absorption fine structure (EXAFS) spectra and pair distribution functions (PDF) from a binary system with several different concentrations of randomly distributed radial, rotational, or buckling static distortions. The PDF and EXAFS are examined to determine if unique signatures for the different distortions can be obtained. It is shown how the complementarity of the PDF and EXAFS data can be used to effectively separate the radial from the rotational local distortions. [S0163-1829(98)04445-2]

I. INTRODUCTION

The application of methods for local structure determination has recently revealed local and medium-range distortion patterns in a number of crystalline materials of scientific and technological interest. The current data analysis protocols for the local structure measurements suffer from the problem of uniqueness. In many cases fitting or modeling of real data to extract structural parameters is improved by the addition of a local distortion, but there is typically ambiguity in elucidating its characteristics. The purpose of this study is to systematically analyze the effects of different types of local structural distortions on extended x-ray absorption fine structure (EXAFS) and pair-distribution functions (PDF) and to test various approaches for extracting unique signatures for them. We study this problem here in simulations of *both* the EXAFS and the PDF of a given structure modified by different local static distortions commonly arising in interpretation of recent experimental data.

The average, long-range structure of crystalline materials is determined with very high precision by Rietveld refinement of Bragg peaks in x-ray and neutron diffraction experiments. The local structure around each element can be probed by EXAFS.[1] A complementary approach to study the local and mesoscale structure is to analyze the diffuse scattering alone or together with the Bragg peaks to obtain pair distribution functions.[2,3] These local structure approaches have recently become possible for crystalline and quasicrystalline materials due to the development of high-flux synchrotron x-ray and neutron sources.

The EXAFS and PDF probes have revealed local distortions in such systems of interest as high-temperature superconductors,[4] colossal magnetoresistance materials,[5–8] metallic alloys,[9] and oxide ferroelectrics.[10] Postulated types of such distortions are buckling or rotation of the oxygen nearest neighbors of the in-plane copper atoms in cuprate high-temperature superconductors[4,11,12] which are believed to coalesce into stripes,[13] polarons (due to charge-lattice coupling), and Jahn-Teller distortions affecting the MnO_6 octahedra in manganese-based perovskite compounds.[5–8] The correct determination of these atomic and possibly nanometer-scale deviations from the average long-range structure is essential for understanding the chemistry and physics of these materials, which usually involve strongly nonlinear phenomena.

The methods for the determination of crystal structures are well established.[14] The lattice parameters and the atomic positions in the asymmetric unit, assuming the periodicity of the lattice, are typically determined with a precision of four to six significant digits. This high precision is possible because of the large number of data points (equivalent to the number of Bragg peaks measured), of the order of 10^3, whereas only of the order of 10^2 are used in the fitting procedure (Rietveld analysis) for a moderately complicated structure with a few tens of atoms in the asymmetric. The number of independent data points in EXAFS is usually of the order of 15 to 30, whereas the number of adjustable variables is of the order of 10. This leads to a considerably smaller number of degrees of freedom in the fitting and a lower precision in estimating distances (usually three significant digits). In addition, the raw EXAFS data pass through a number of operations (background removal, determination of the threshold energy E_0, Fourier filtering with specific weight and window functions multiplying the data, etc.) before the final fitting is done to determine the structural parameters. Therefore, it is important to compare the results obtained from analyzing EXAFS data by various techniques with the actual structures which determine the spectra. We do this here by the use of a model three-dimensional (3D) crystal structure into which we can incorporate different types and quantities of local distortions.

We also calculate the radial pair distribution functions for the same structures. The analysis of PDF's and static structure factors (total and diffuse) in 2D systems has been discussed elsewhere.[15] Radial PDF's are currently determined in experiments by measuring the total static structure factor $S_{\mathrm{tot}}(Q)$ (the sum of the Bragg and the diffuse scattering) for

powder samples and Fourier transforming it from momentum to real space:[2,3]

$$G_{\mathrm{tot}}(r)=1+\frac{1}{2\pi^2 nr}\int_0^\infty [S_{\mathrm{tot}}(Q)-1]\sin(Qr)Q\,dQ, \quad (1)$$

where $n=N/V$ is the average number atomic density. Powder samples effectively average out the angular degrees of freedom in $S_{\mathrm{tot}}(\mathbf{Q})$. Experimentally, $S_{\mathrm{tot}}(Q)$ is measured over a finite Q interval. Since $S_{\mathrm{tot}}(Q)\rightarrow 1$ as $Q\rightarrow\infty$, an accurate determination of $G_{\mathrm{tot}}(r)$ requires sufficiently large values of Q. This is typically[2] $Q\geqslant 3/\sigma_r$, where σ_r is determined from the Debye temperature factor[16] $\exp(-Q^2/\sigma_r^2)$. Values of $Q_{\max}\approx 45$ Å^{-1} are achievable in pulsed-neutron scattering. The raw neutron scattering data is usually corrected for absorption, inelasticity effects, and multiple scattering before the Fourier transform in Eq. (1) is calculated to obtain the PDF. If the PDF is known, the number of atoms z in a shell contained in an interval of distances $r_{\min}\leqslant r\leqslant r_{\max}$ from an atom at the origin can be calculated from

$$z=4\pi n\int_{r_{\min}}^{r_{\max}} G_{\mathrm{tot}}(r)r^2 dr. \quad (2)$$

The PDF data analysis is performed[2,3] either by analogy with the Rietveld method (''real-space Rietveld'') or by using a simulated annealing method. In either case, the average structure in terms of lattice parameters, temperature factors, atom positions, and occupancy factors can be refined. The great advantage of the PDF method over the q-space Rietveld refinement is the automatic inclusion of the diffuse scattering which accounts for structural distortions intrinsically.

EXAFS and radial PDF methods have in common that they both determine the distances separating pairs of atoms and the numbers of each type of unique pair. However, there are several important differences between the two techniques. EXAFS probes the atomic distribution around each aelement separately, selected by the absorption edge measured, and thus deconvolutes the total PDF into the individual, element specific PDF's. Polarized EXAFS on oriented samples could give additional separation of the components of an element specific PDF based on the angle between the vector connecting the pair and the beam direction, providing additional information for obtaining structural parameters. In determining the type of neighboring atoms composing a specific shell, whereas PDF only has the peak intensities from which to derive this, the EXAFS has a phase as well as an amplitude for identification of the scatterer Z. This phase is also modified by anharmonic pair distributions, so that missing amplitude can be traced back to its source. Finally, the strong scattering of the photoelectron results in waves in the EXAFS originating not only in actual neighbor shells but rather from multiple scattering paths. While this rapidly increases the complexity of the EXAFS with distance, it nevertheless also provides a means for extracting the angular information essential in discriminating between various types of defects. The PDF (e.g., from neutron scattering), however, can be well determined to longer distances than from EXAFS thus allowing the differentiation of the short and the medium-range order in a given structure. The longer range of the PDF gives a good test for the propagation of local distortions and thus increases the level of confidence in their determination.

The PDF (using a definition suitable for the real-space analysis of the neutron scattering data) is the sum of the partial pair distribution functions

$$G_{\mathrm{tot}}(\mathbf{r})=\sum_{i,j}\frac{b_i b_j}{\overline{b}^2}c_i c_j G_{ij}(\mathbf{r}), \quad (3)$$

where $c_i=N_i/N$ is the concentration and b_i is the scattering length of the ith component (the sum is over the different components in the system and $\overline{(\ )}$ denotes compositional average). The partial PDFs are

$$G_{ij}(\mathbf{r})=\frac{V}{N_i N_j}\sum_{k=1}^{k=N_i}\sum_{l=1}^{l=N_j}\langle\delta(\mathbf{r}-\mathbf{r}_{kl})\rangle, \quad (4)$$

where $\langle\ \rangle$ represents ensemble average and $\mathbf{r}_{kl}=\mathbf{r}_k-\mathbf{r}_l$. It is more complicated to isolate the local environment of a specific type of atom from the PDF since the peaks from all atomic pairs at similar distances will be present.

II. MODELS FOR LOCAL DISORDER AND SIMULATIONS

We consider a binary cubic structure of the type AB_3 with a unit cell shown in Fig. 1. The A atoms are positioned in the corners of a cubic unit cell and the B atoms are in the centers of the edges. Each A atom is surrounded by an octahedron of B atoms. This is a generic structure which allows us to model different types of octahedral distortions currently discussed in mixed valence, electronically active, perovskite type compounds such as high-temperature superconductors, ferroelectric, and colossal magnetoresistance oxides. This model is thus an excellent choice to develop insight and intuition for different defect signatures in this class of materials.

For example, Billinge *et al.*[12] have studied the low-temperature tetragonal (LTT) to low-temperature orthorhombic (LTO) phase transition in $La_{2-x}Ba_xCuO_4$ by PDF analysis. They have shown that the data can be fitted well by rigidly tilting the CuO_6 octahedra on a *local* scale in the [110] (LTT) direction in both phases. This differs from the models used to fit the structure by tilting the octahedra in the [010] direction in the LTO phase.

Different types of local octahedral distortions appear in analyses of measurements on the perovskitelike compounds $La_{1-x}A_xMnO_3$ (where A is substituted by a divalent ion Ca, Sr, Ba). These are colossal magnetoresistance materials[17] (CMR) which have paramagnetic insulator (PMI) and ferromagnetic metal (FMM) phases at high and low temperatures, respectively. Millis *et al.*[18] suggested that both double exchange and Jahn-Teller effects have to be considered to explain the physics of the manganites. They proposed that the Jahn-Teller effect will induce very strong electron-phonon coupling leading to small polaron formation.[19] The formation of polarons has been tested by using EXAFS and PDF to measure the oxygen displacements of the MnO_6 octahedra in manganite materials at different doping concentrations.

Billinge *et al.*[7] considered only the nearest neighbor O-O bond in $La_{1-x}Ca_xMnO_3$ by PDF analysis of neutron diffraction data as a function of temperature at three different dop-

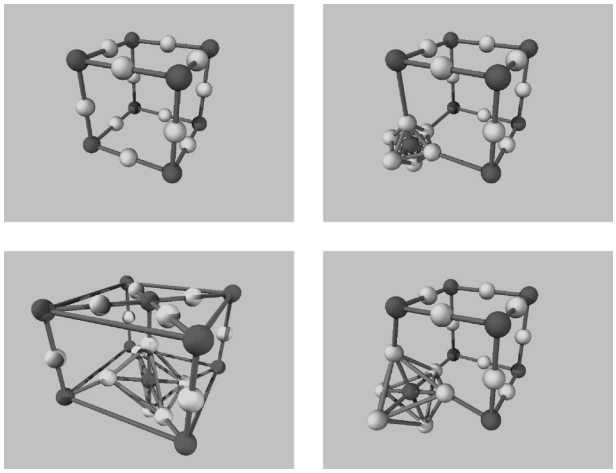

FIG. 1. The cubic unit cell of the AB_3 long-range order structure (top left) and some of the local distortions affecting AB_6 octahedra considered: breathing mode (top right), buckling (bottom left), rotation around the [010] axis (bottom right).

ing concentrations. They modeled the polaron formation in the PMI phase by a static breathing mode oxygen distortion, i.e., polaron-distorted MnO_6 octahedra of Mn^{4+} ions, mainly introduced by the doping of La^{3+} with divalent cations. The oxygens were calculated to be uniformly collapsed toward the corresponding Mn^{4+} by 0.12 Å. However, the analysis of this peak may be incomplete since pair correlations of atomic types different from the O-O pairs, e.g., La-O and Ca-O, contribute at similar distances. A different approach to detect polarons in $La_{1-x}Sr_xMnO_3$ has been used by Louca *et al.*[8] They found evidence for a strong Jahn-Teller effect distorting the MnO_6 octahedra of Mn^{3+} ions, leading to two long and four short Mn-O bonds in both the PMI and FMM phases, by PDF analysis of only the nearest neighbor Mn-O bond. The polarons at room temperature are again considered as localized on Mn^{4+} ions leading to six Mn-O bonds with equal lengths. Since at 10 K the number of Mn-O bonds reaches six at lower doping concentration ($\approx 35\%$) than in the pure $SrMnO_3$ (as measured at room temperature), they argued that the polaron is extended over approximately three Mn sites. In addition, Rietveld analysis of neutron diffraction data[20] has been interpreted as showing that the MnO_6 octahedra are globally tilted with a maximum tilting angle between MnO_6 octahedra (the Mn-O-Mn angle) in the monoclinic phase of $LaMnO_{3+\delta}$ equal to 160.1°, making the analysis of the polaron distortions even more complicated.

In order to study the specific signatures of such types of distortions, we have calculated the EXAFS and PDF's of the cubic AB_3 structure with random distributions of local distortions affecting only the *B* atoms of AB_6 octahedra. In our model crystal, the *A*-*A* nearest neighbor distance is set equal to 4 Å, which is conserved independent of the distortions because they do not affect the *A* atoms. In the undistorted cubic unit cell, the *B* atoms have been placed midway between adjacent *A* atoms, giving an *A*-*B* bond equal to 2 Å. The choice of $A=$Mn and $B=$O and distances close to those found in the manganites (this is actually of no importance since all distances scale) will give signatures in the EXAFS and PDF which would occur for those proposed for the MnO_3 sublattice in manganese-based CMR oxides. We studied five types of static local distortions emulating those which have been proposed for this class of mixed valence transition metal oxides.

(a) Displacement (breathing mode) defect—the six *A*-*B* bonds of a distorted AB_6 octahedron are contracted by 0.1 Å towards the *A* site (simulates a small polaron). An example of such a distorted octahedron is shown in Fig. 1.

(b) Extended (displacement) defect—the nearest neighbor *B* sites of a central *A* site and the *B* sites forming the nearest neighbor octahedra of the central AB_6 octahedron are displaced. The *A*-*B* bonds of the central AB_6 octahedron are reduced by 0.12 Å moving the *B* sites towards the central *A* site and the *A*-*B* bonds of the nearest neighbor octahedra (excluding the shared and already displaced *B* sites) are reduced by 0.08 Å in similar displacements of the *B* sites towards the corresponding centers (*A* sites) of these octahedra. There are a large number of different lengths involved in this extended defect.

(c) Buckling local defect—the four *B* sites (in *XY* planes) of each of the distorted AB_6 octahedra receive small out-of-plane displacements; two of them are displaced above the plane and two below it (see Fig. 1). The out of plane displacements are chosen such that the buckling angle [defined as $180°-\angle(ABA)$, where $\angle(ABA)$ is the angle at a buckled *B* site] is equal to 12°.

(d) Rotational local defect—AB_6 octahedra are rotated around the [010] axis (Fig. 1).

(e) Rotational local defect as in (d) but with an axis of rotation along [110].

In all of these cases we have used a ''hard sphere'' approach (i.e., defects do not overlap) to randomly distribute different types of distortions at a set of concentrations. To avoid problems associated with overlapping defects, when an *A* atom was selected as a center of a defect its six *A* nearest neighbors were excluded as sites for subsequent defect centers. The concentration of local defects is defined as the fraction of the number of *A* site centers of such defects to the total number of *A* sites in the system. Note that there is an upper limit on the concentration of local defects which can be randomly distributed due to the excluded volume effect and that the concentration of local defects, for the values considered here, is approximately equal to the optimal doping level in Mn related CMR compounds. The extended defect is constructed similarly. Because it involves seven *A* and 36 *B* atoms, in this formulation the extended defect is similar to seven of the local defects. In constructing the model crystal with the extended defects, such defects were incorporated only about one seventh as many times as for the local defects so that the same number of *A* atoms were locally distorted AB_6 octahedra for all cases of a particular defect concentration.

The radial PDF and the EXAFS are calculated on a system comprising $L\times L\times L$ unit cells with periodic boundary conditions applied. Three system sizes have been used in the simulations with a total of 16^3, 20^3, and 32^3 particles, with the larger systems used for lower defect concentrations to ensure accurate sampling. The size of the system also depends on the maximum distance $r_{\max}$ for which the PDF is calculated with the requirement $L/2>r_{\max}$, assuming periodic boundary conditions. We used a histogram algorithm[21] for the calculation of the radial PDF.

The simulation proceeds by first distributing the atoms on their lattice positions. Then the defects are randomly distributed through the crystal up to the specified concentration. Finally, random displacements are added to all atoms to model thermal displacements. The partial PDF's, $G_{ij}(r)$ [Eq. (4) with $i,j=A,B$], are calculated and averaged over the different distributions of local defects in the system (the static distortions) and the thermal random displacements of the particles. We used Gaussian random displacements with equal standard deviations for both the A and B particles ($\sigma_i = 0.04$ Å, $i=x,y,z$). An average over 100 distributions of defect and ''thermal'' displacements already gives sufficiently smooth curves.

The choice to model the thermal displacements of atoms by sampling their positions according to a given distribution function allows, in general, to probe an arbitrary asymmetric distribution of these displacements. This is not possible with the currently used methods to model the experimentally measured PDF's (Refs. 2 and 3) in which the thermal displacements are accounted for by a convolution of a PDF calculated from the the average positions in the unit cell. The convolution function is Gaussian with at most three different Debye-Waller factors (along each direction in space). The Gaussian function comes from the traditionally used form of the Debye-Waller factor $W(\mathbf{Q})=Q^2\langle \mathbf{u}^2\rangle/2$, where $\langle \mathbf{u}^2\rangle$ is a mean square displacement of a nucleus. In general, the Debye-Waller factor in crystalline materials is anisotropic and will depend on the direction of the scattering vector $\mathbf{Q}$ (it is isotropic in $\mathbf{Q}$ only in cubic crystals). Thus, to explain asymmetric peaks in the PDF a direct calculation of the Debye-Waller factor for each value of $\mathbf{Q}$ should be performed using the phonon frequencies and polarization vectors and, if necessary, anharmonic effects should be taken into account as well. Note that asymmetric peak shapes can also be caused by the resolution function of a given experimental instrument.[3] For example, in some time-of-flight neutron instruments the resolution function is a Gaussian with a standard deviation which is proportional to the magnitude of the scattering vector Q. The separation of the static from the thermal disorder would then require study of the difference between the experimental data and a theoretical calculation based on the phonons for a given material. For modeling purposes, however, the method to sample a prescribed distribution of particles should directly allow investigation of asymmetry in materials with highly bond-oriented order.

In EXAFS, the ''Debye-Waller factor'' is defined differently than in diffraction. The scattering vector is replaced by the vector connecting the equilibrium positions of a pair of atoms and it also includes the correlation effects of the displacements of the atoms in the considered pair[22] (these correlations are treated in diffraction in the inelastic part of the scattering). Non-Gaussian peak shapes are studied mainly by choosing an asymmetric *radial* PDF, i.e., the angular averaging has been assumed, which is expanded in cumulants and a relevant number of odd order coefficients are used to model the peak shape and position.[23] The even order coefficients contribute to the Debye-Waller factor. Generally, the calculation of the EXAFS Debye-Waller factor should also be done using the phonons of the considered system. Nevertheless, the method we describe below for the calculation of the EXAFS based on distribution of particles is directly applicable to model asymmetric distributions in the same consistent way as in the calculation of the PDF. Certainly, the availability of additional structural measurements which are very weakly affected by the thermal disorder, such as x-ray absorption near-edge structure (XANES), should considerably help in the separation of the static from the thermal disorder.

The multiple scattering calculation of the EXAFS is based on the FEFF7 code.[24,25] This code is mainly used to generate scattering paths, amplitudes and phases, from a single absorbing atom with a few tens of surrounding atoms in order to provide theoretical standards in the process of fitting experimental data. While this is certainly appropriate in the analysis of isotropic or crystalline structures since it assumes a single average site, it will not give a complete description of a structure with defects. The oscillatory part of the absorption coefficient

$$\chi(k)=\frac{\mu(k)-\mu_0(k)}{\mu_0(k)}, \tag{5}$$

where $\mu(k)$ and $\mu_0(k)$ are the absorption coefficients from the given structure and the structureless background, respectively,[1] contains contributions from all possible absorbing atoms. Absorbers with various local environments due to distortions will have different scattering geometries. We accounted for this effect in calculating $\chi(k)$ by averaging over an array of A absorbing sites which effectively accomplishes an average over the different scattering configurations. First, FEFF7 is run to calculate $\chi(k)$ for each absorber specified (we used 121 absorbers in these calculations), and then the calculated $\chi(k)$'s are averaged to obtain the final $\chi(k)$. The positions of the absorbing atom and a cluster of atoms within a sphere with a given radius and a center located at the position of the absorber are given as input to FEFF7 in the calculation of $\chi(k)$ for each absorber. The magnitude of the radius used was in the range from 10 to 14 Å. The calculated, configurationally averaged, $\chi(k)$ can be used to directly fit $\chi(k)$ determined experimentally on an unknown structure. This eliminates the systematic errors of one or two Fourier transformations of polynomially weighted and windowed data before the final fit is performed. However, we use configurationally averaged $\chi(k)$ here to theoretically study the signatures of a priori prescribed local and extended static distortions.

Since the MnO_3 sublattice was used as a prototype of the AB_3 binary structure, the scattering lengths of the A and B atoms were set to these corresponding to manganese and oxygen, respectively, in the calculation of the PDF's. Note that the scattering length of Mn is negative while for O it is positive leading to negative intensities of the Mn-O peaks in the PDF defined by Eq. (3). The calculated EXAFS are from the K edge of Mn with potentials for manganese and oxygen.

III. RESULTS

A. PDF

The concentration dependence of the total PDF's for the different types of distortions described in the previous section are shown in Fig. 2. The breathing mode local defect affects most the first negative and positive peaks due to A-B

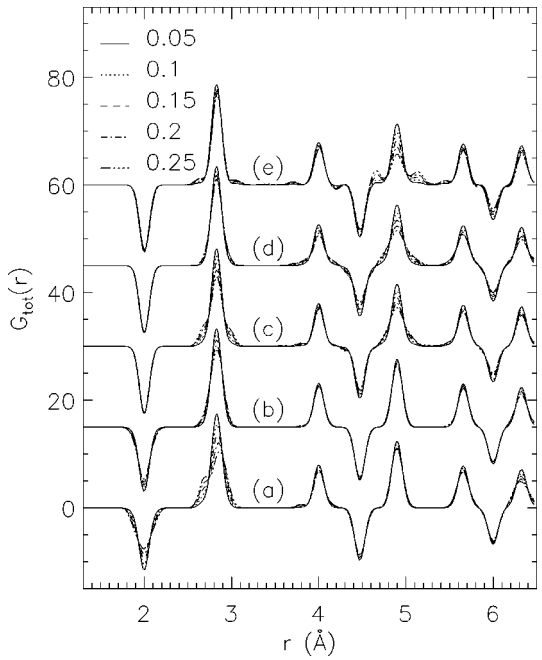

FIG. 2. The total pair distribution function for a set of concentrations (0.05 to 0.25) of randomly distributed distortions: (a) breathing mode local defects, (b) cluster defects (see text), (c) buckling with a buckling angle of 12°, (d) rigid octahedral rotations at 6° about the [010] axis, and (e) about the [110] axis. An offset of 15 along the *y* axis has been applied starting with case (b) in order to fit the sets of data on the same plot. Note that the definition we used for the PDF makes it dimensionless. The (a) to (e) notation will be the same on all following figures which contain it.

and *B*-*B* nearest neighbor (NN) pair correlations, respectively. Since each such defect changes 12 NN *A*-*B* bonds at an initial length of 2 Å to six short at 1.9 Å and six long at 2.1 Å, this peak consists of pair correlations at these three bond lengths. Due to the thermal broadening, these three peaks cannot be resolved and their intensities depend on the concentration of local defects present in the system. The intensity of the main peak at 2 Å decreases when increasing the concentration of the defects and the increase of the intensities of the peaks at 1.9 and 2.1 Å appear as broadening of the tails of the main peak.

The effect on the *B*-*B* NN peak is similar but slightly more complicated. Each defect will change the 12 *B*-*B* bonds of the affected AB_6 octahedron from $2\sqrt{2}$ to $1.9\sqrt{2}$ Å, while the *B*-*B* bonds of the defect *B* sites with the NN octahedra will change to bond lengths of $\sqrt{2.1^2+4}$ and/or $2.1\sqrt{2}$ Å, depending, respectively, on the absence or presence of other distorted octahedra centered at next NN *A* sites. As expected, the decrease of the intensity of the peak at $2\sqrt{2}$ Å will lead to an increase of the intensities of the peaks at the additionally created *B*-*B* NN bond lengths with the increase of the peak intensity at $1.9\sqrt{2}$ Å starting to resolve as a separate peak from the main one. The number of bond lengths at $1.9\sqrt{2}$ Å is larger than any of the corresponding numbers at the other two bond lengths created by the presence of the defects which are also at a greater r. In this definition of the PDF, for two peaks at different values of r but including the same number of atoms, the peak at smaller r will have higher intensity [see also Eq. (2)]. The signatures of the different

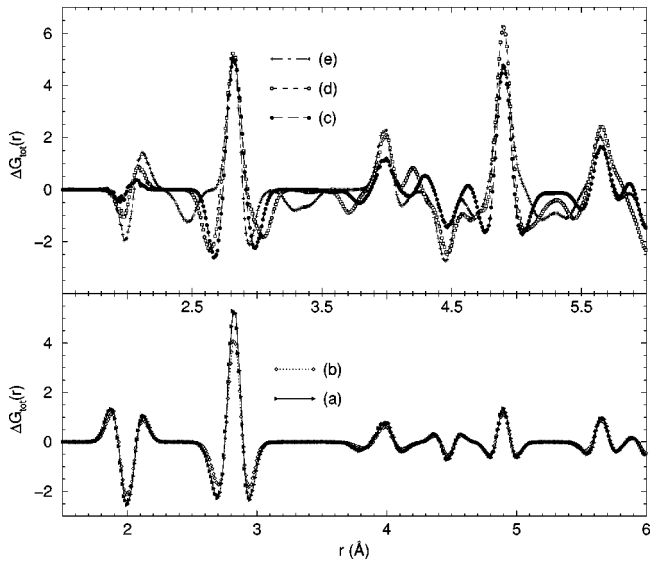

FIG. 3. The differences $\Delta G(r)=G_0(r)-G(r)$ vs r of the PDF $G_0(r)$ for the ordered structure and the PDF's $G(r)$ for the structures with the static displacements. The $G(r)$ PDF's are calculated for a system of 32^3 particles and 0.2 concentration of local defects. The buckling angle for (c) is 12° as are the rotational angles for (d) and (e).

defects in the PDF are better compared by presenting the difference between the PDF $G_0(r)$ of the original ordered structure and the PDF $G(r)$ of the structures with the defects (Fig. 3). It is clear that the decrease of the intensity of the first two main peaks in Fig. 2 for the (a) set of curves will be linear with the increase of the concentration of the defects, as can also be seen in Fig. 4, due to the specific nature of their distribution (see the previous section). From the slope of these curves the number of *A*-*B* bonds at shorter distances than in the long-range structure can be determined. We consider below a different method to extract the same number from the EXAFS data.

The propagation of this local distortion also affects the next peaks in the PDF but, as expected, to a much smaller extent. Note the small decrease of the intensity of the peak at

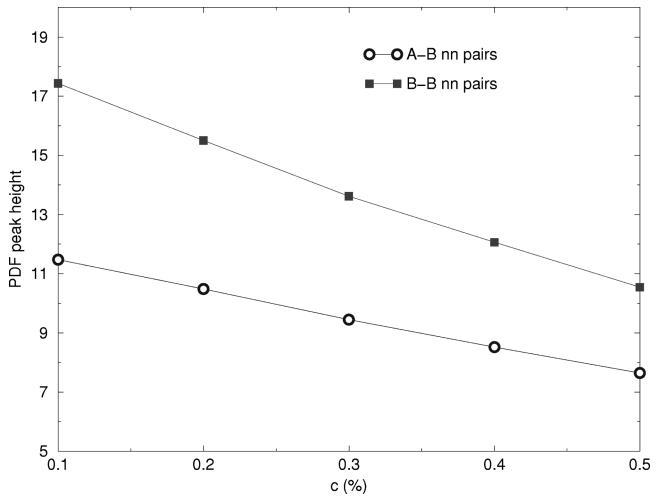

FIG. 4. Dependence of the intensities of the first two peaks in the total PDF on the concentration of breathing mode distorted AB_6 octahedra.

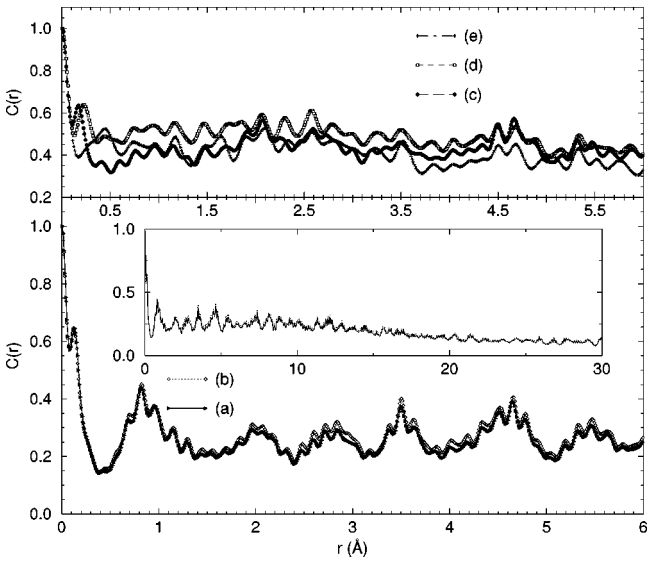

FIG. 5. Correlation function based on the magnitude of the PDF differences (see text for the definition) for the same set of simulations as in Fig. 3. The inset in the lower part of the figure contains the correlation function for the (a) and (b) cases up to 30 Å.

4 Å for the (a) set of curves in Fig. 2. The total PDF has contributions from *A-A* and *B-B* pair correlations at this distance. The lack of the partial PDF's makes it difficult to determine which of these two types of pair correlations, or both, causes the change in this peak. The availability of the *A* EXAFS spectra, *in addition* to the PDF's, resolves this and allows assignment of the changes in the PDF as due only to displacements of *B* atoms.

The PDFs of the clustered distortions [Fig. 2(b)] show the local distortions within the cluster in the first two peaks similar to the breathing mode distortions. However, in this case the changes in the first two peak intensities are smaller since most of the *B* sites are displaced by 0.08 Å and a considerably smaller number by 0.12 Å. The linear size of the clusters is approximately 8 Å. While the calculation of the PDF on a length scale several times the size of the clusters is straightforward, we still do not have a clean method to determine the cluster size correlations in the PDF. This is due to the sensitivity of the PDF, which is most suited to studying correlations at small r. The differences $\Delta G(r)$ for the cluster defects shown in Fig. 3 are also very close to the case of breathing local distortions. Generally, these differences will be correlated and one may expect to be able to determine the magnitude of the local distortions and the size of the cluster defect from a suitable correlation function. We have considered the following correlation function:

$$C(r)=\frac{\Sigma_{i=0}^{N}|\Delta G(r_i)|\times|\Delta G(r_i+r)|}{\Sigma_{i=0}^{N}[\Delta G(r_i)]^2}, \tag{6}$$

which is shown in Fig. 5. The highest frequency of oscillations in the correlations of the differences is approximately equal to the magnitude of the static displacements. Thus, rather than trying to determine this number only from fits to the experimental data, such a correlation function can be used as a first indication of the magnitude of local static distortions in a system. The inset in the lower plot in this figure gives the correlation function up to 30 Å for the breathing and cluster distortions. Generally, the PDF for the cluster defects contains information on the size of the cluster on this length scale. In this case the two curves are very close and it is very difficult to differentiate the cluster from the local defects. The diffuse scattering part of the static structure factor $S_{\mathrm{diff}}(q)$ may be the best probe for the determination of the cluster size, since $S(q)$ is most sensitive to structure at small q, i.e., large r. We expect[15] to be able to make such analysis of $S_{\mathrm{diff}}(q)$ in 3D and results on simulations of the diffuse scattering will be reported elsewhere.

The PDF for the buckling and two rotational local distortions also cause a change (Fig. 2) of NN *A-B* bonds, but this change is approximately 0.01 and 0.02 Å. It is clear from the figure that these bond lengths cannot be resolved and the first peak at approximately 2 Å appears unchanged by the presence of the defects. However, the plot of the differences $\Delta G(r)$ in Fig. 3 shows that this peak is also affected by the distortions in an asymmetric way [the (c) to (e) curves], which is quite different to the differences observed for the radial distortions [(a) and (b) curves]. The main effect in the PDF is observed in the second peak due to NN *B-B* correlations. This is also the main difference with the previous two cases of radial defects where the first peak was strongly affected by the defects. We shall see that the availability of the EXAFS data on the same five cases allows us to distinguish the rotational from the radial distortions, as well as that the static distortions are present only for the *B* atoms. The buckling and the rotational types of local defects change the PDF in a very similar way since the differences in the PDF's are very small. However, once the type of distortion (rotational or radial in our case) has been determined qualitatively, the currently practiced[2,3] refinement of the PDF will show which of several proposed distortions is the best fit to the experimental data. The correlation function $C(r)$ for these types of distortions also gives a very good estimate of the magnitude of the local static distortions (see Fig. 5).

B. EXAFS

The magnitudes $|\chi(r)|$ of the Fourier transformed $\chi(k)$ [Eq. (5)]

$$\chi(r)=\int_{k_{\min}}^{k_{\max}} e^{-2ikr}W_{\alpha}(k)k^{n}\chi(k)dk, \tag{7}$$

with $n=3$ and a Gaussian window function $W_{\alpha}(k)$, for the same cases of distortions as in Fig. 2 are shown in Fig. 6. The k-space range of the Fourier transform was fixed at $3.8 \leqslant k \leqslant 15.3$ Å^{-1} (the typical range in the Fourier transform of experimental data is usually 3 to 15 Å^{-1}) and the Gaussian window function margins were equal to 0.5 Å^{-1}. The peaks in $|\chi(r)|$ from a given edge correspond to the different coordination shells of the specific absorbing atoms and thus give more detailed information concerning the correlations involving these type of atoms than the total PDF which contains all atomic type pair correlations. The dependence of $|\chi(r)|$ on r is only qualitatively similar to the PDF's. The $|\chi(r)|$ peaks are shifted to lower values of r than their actual positions, by approximately 0.2 to 0.5 Å^{-1}, an amount due to the scattering shifts of the photoelectron, the specific elements involved, the weighting scheme, etc.

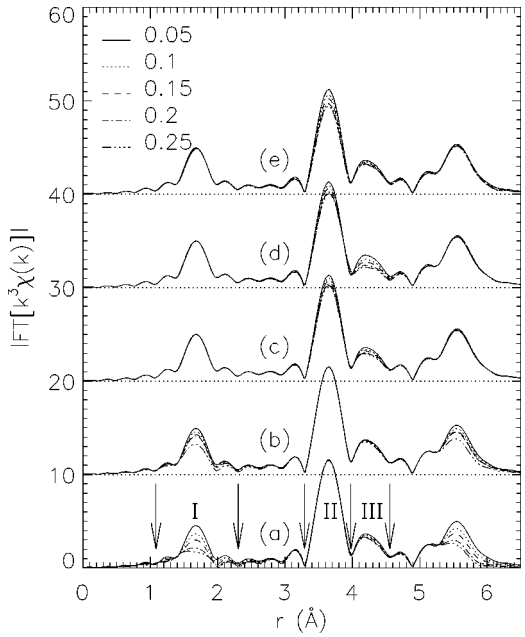

FIG. 6. Magnitude of the Fourier transform of $k^3\chi(k)$ vs r for the same cases of local distortions as in Fig. 2. An offset of 10 along the y axis has been applied starting with the (b) set of curves. The regions marked I to III are also Fourier transformed back to k space to study the phase shifts (see below) associated with them.

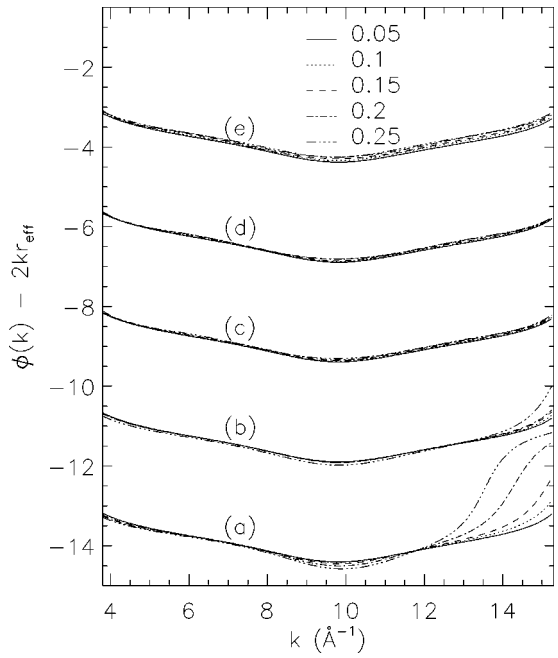

FIG. 7. Phase shifts from back to k-space Fourier transform of the r-space filtered data in the range $1.084 \leqslant r \leqslant 2.305$ Å (the I region in Fig. 6) and $r_{\text{eff}} = 1.693$ Å. The y-axis offset is 2.5.

Since the $\chi(k)$'s were calculated for an edge of the A atoms (K edge of manganese used for the A atoms with oxygen substituted for the B atoms), the first peak at ≈ 1.679 Å represents NN A-B correlations and the second at ≈ 3.634 Å is mainly due to single scattering from the A NN of the absorbing A atom. However, there are also contributions from multiple scattering paths involving intervening B atoms which will modify the A NN χ. Similarly to the PDF's in Fig. 2, the magnitudes of the first shell peak decrease when increasing the concentration of defects with radial distortions [Figs. 6(a) and 6(b)] and are essentially unchanged for the buckling and rotational distortions. The comparison of the (a) or (b) set of curves in Fig. 2 for the PDF's and in Fig. 6 for the EXAFS show that the decrease of the amplitude of the peak at 4 Å observed in Fig. 2 should only be caused by displacements of the B type of atoms at similar distances since the A-A type of correlations at the same distance are not affected by the presence of static distortions.

The first shell peak in the EXAFS remains approximately unchanged for buckling and rotational distortions [Figs. 6(c)–6(e)] as in the PDF's but the intensity of the second peak due to A-A NN backscattering is reduced. If this was due to static displacements of A atoms then we should observe a similar effect in the first peak as well, since distortions in the average positions of the A atoms will also affect the NN A-B bond. The observed behavior can readily be understood assuming rotational displacements of the NN B atoms, or small buckling deviations, which does not essentially change the first peak but affects the second peak due to the contributions of multiple scattering. The intervening B atoms in the multiple scattering paths for the distances in the second peak are out of the collinear paths, which will lead to a decrease of the scattering amplitude.[27,22] An example to determine small buckling angles from this multiple scattering effect is given below.

The signatures of the local distortions also appear in the EXAFS phase shifts (Figs. 7 to 9 for the regions marked I to III in Fig. 6). The phase shift is defined as the phase of a back Fourier transform over an r-space interval containing a peak or a set of unresolved peaks minus the $2kr_{\text{eff}}$ factor (see, e.g, Ref. 22). The phase shifts are strongly correlated to the relative atomic distances and should be more sensitive to the changes in r than $|\chi(r)|$. Moreover, the amplitudes in experimental data are easily distorted by noise or analysis artifacts. Although this is not one of the conventional means for analysis of EXAFS data, it is worth testing because of its sensitivity to small distortions. In combining the waves from two or more paths, the material itself provides an excellent diagnostic by inspection of the beat regions in the resulting $\chi(k)$. Different types of distortions may effect different patterns of responses in sets of phase shifts taken over several regions in real space.[26]

The EXAFS phase shifts of the first shell from the back-transformed Fourier filtered data are shown in Fig. 7. As expected, the main changes in the phase shifts are observed for the radial displacements and in particular for the (a) set of curves where all static displacements are of magnitude 0.1 Å. Increasing the local defect concentration in this case will increase the amplitudes of the two A-B correlations at 1.9 and 2.1 Å and decrease the amplitude of the undistorted one at 2 Å. This increase will eventually lead to a well characterized beat, splitting of the first shell peak, and the deviations observed in the phase shifts. The effect on the phase shifts due to the extended defect is smaller since, as discussed in the PDF results above, this is now a more complicated, five-site distribution. The cases of buckling and rotational local defects show virtually unchanged first shell phase shifts, when varying the defect concentration, indicative of the very small changes in the A-B distances of 0.02 and 0.01 Å, respectively.

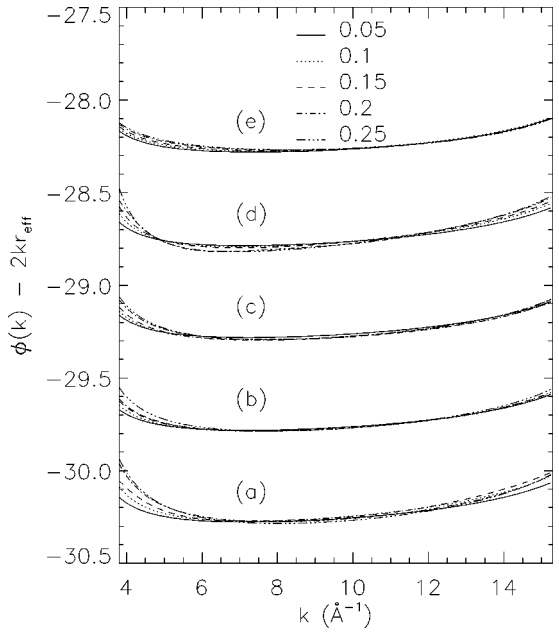

FIG. 8. The phase shifts from the back Fourier transformed r range II in Fig. 6 ($3.289 \leqslant r \leqslant 3.978$ Å, $r_{\mathrm{eff}} = 3.635$). The y-axis offset is 0.5.

The phase shifts from the back Fourier transform of the data in the second peak of the EXAFS are shown in Fig. 8. While the k dependencies of these phase shifts are qualitatively similar to each other, there are nevertheless small differences for the various types of distortions. The behavior of the phase shifts for the third region (marked by III in Fig. 6) are presented in Fig. 9 and in this case the differences among the various types of defects are larger than in Fig. 8. The specific propagation of these differences seen in Figs. 7 to 9 show that, in principal, the potential exists to distinguish among these possible static distortions by contrasting the behavior of the phase shift from subsequent regions in r space with the corresponding ones from the data. Buckling and rotations are particularly important in this respect since such distortions reduce the focusing effect by decreasing the contributions of the three and four leg scattering paths in quasicollinear atomic arrangements leading to overall smaller scattering amplitudes and changes in the scattering phases.

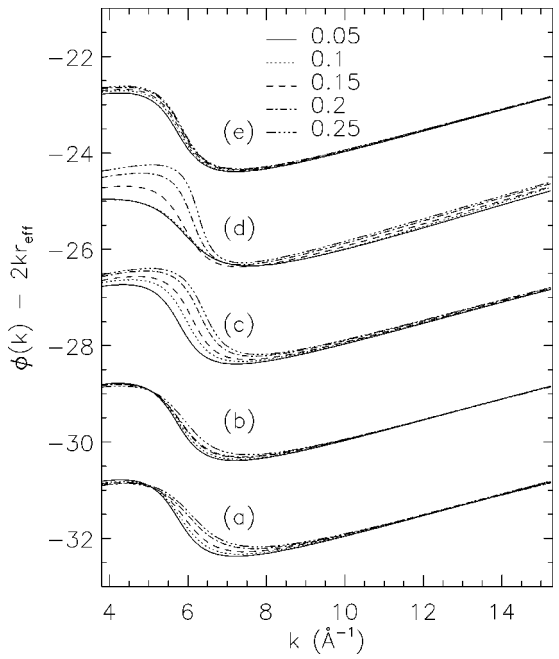

FIG. 9. Phase shifts of the back Fourier transformed r range $3.978 \leqslant r \leqslant 4.555$ Å and $r_{\mathrm{eff}} = 4.141$ Å (region III in Fig. 6). The y-axis offset is 0.5.

There are two cases for which we have also performed fits to extract quantitative information regarding the change of the structural parameters due to the distortions. The calculated, configurationally averaged $\chi(k)$ contains contributions from absorbers with undistorted positions of nearest and next nearest neighbor atoms as well as from absorbers at local distortions. The scattering paths from these different local configurations will mostly affect the EXAFS data for the first few shells. Generally, the fitting of data on crystalline structures with large static disorder (0.08 Å or greater) with only Gaussian broadened shells will not work (but see Ref. 6 for an example of such a study); Gaussian broadened shells give good fitting results when assuming an average structure with resolution better than the broadening interval. It will be necessary to generate scattering paths for the structures with large static distortions from the expected different local configurations and use them with proper weights in the fitting procedure. The effect of multiple scattering should also be considered. We used FEFF to generate such paths from several absorbers with different local configurations of atoms and usually about twenty paths are sufficient in the fitting of the first few shells.[25] These paths are then used as input to the FEFFIT program[28] to make constrained fits of the configurationally averaged $\chi(k)$.

The concentration of breathing local distortions can be determined from a constrained fit of the first peak in the EXAFS with weighted contributions from shells at 1.9, 2.0, and 2.1 Å. After generating these single scattering paths from running FEFF on three different absorbing A atoms with their NN B atoms at these distances, they are used with weighting factors of x for the paths at 1.9 and 2.1 Å and $6 - 2x$ for the path at 2.0 Å. This reflects the reduction of intensity from the 2.0 Å shell to the other two shells created by the local distortions. The weighting factor x is used as a fitting variable and it will give the contribution of the scattering paths at 1.9 and 2.1 Å consistent with the way the defects are distributed. The total coordination number in the first peak is constrained to 6 as it can readily be calculated from integrating the intensity of this peak in the PDF. The fitting was done in r space and the parameters for the Fourier transform were $2.7 \leqslant k \leqslant 18.0$ Å^{-1}, k weighting, Hanning window function with margins of 2 Å^{-1}. The fitted r space interval was $0.5 \leqslant r \leqslant 2.5$ Å. These parameters led to 18 independent data points which were fit with five variables.

The $|\chi(r)|$ for the data and a typical fit in the case of 15% concentration of local defects are shown in Fig. 10. The initial value $x_{\mathrm{guess}} = 0.7$ was used for the number of atoms in the shells at 1.9 and 2.1 Å and the value obtained in the fit was $x_{\mathrm{fit}} = 0.92 \pm 0.047$, while the actual number is 0.9. The errors in FEFFIT are determined from the reduced χ^2_ν statistics, but because the errors in the data points are not usually well determined χ^2_ν is rescaled before the errors are calculated provided the fit is considered good.[28,29] For initial values

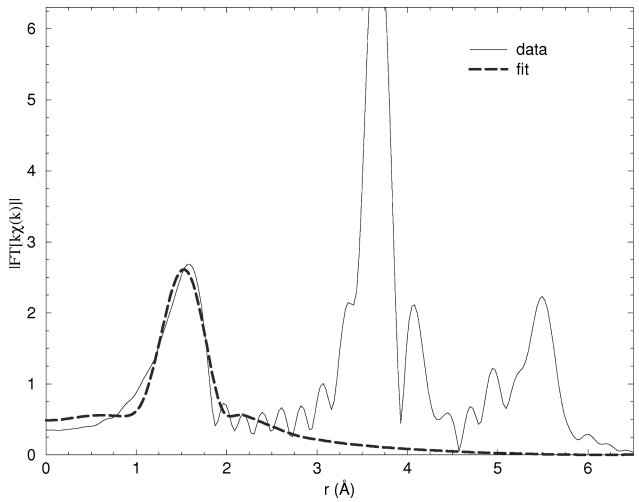

FIG. 10. Magnitude of the Fourier transform of $k^2\chi(k)$ vs r for the breathing mode local distortions at 15% and a constrained fit with three shells for the first peak to determine the number of nearest *A*-*B* neighbors at each of these three shells at distances of 1.9, 2.0, and 2.1 Å. The range of the fit in r space was $0.5 \leqslant r \leqslant 2.5$ Å.

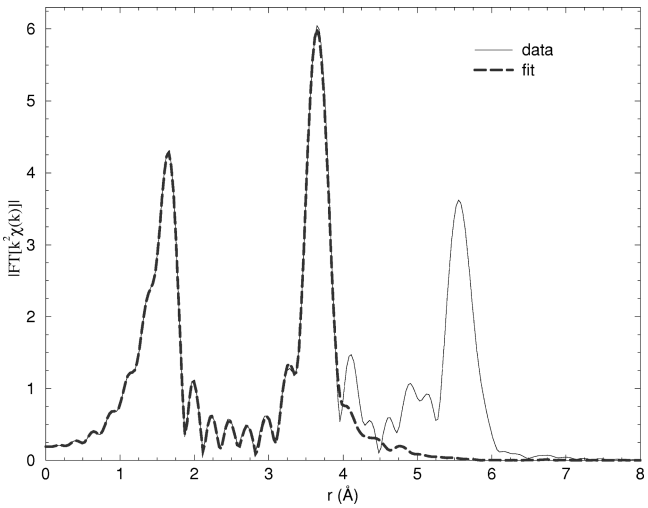

FIG. 11. Magnitude of the Fourier transform of $k^2\chi(k)$ for a structure with buckled *B* sites (the buckling angle is equal to 10°) in the *XY* planes and a constrained fit to it (up to a maximum distance of 4.1 Å) to determine the buckling angle using the contribution of the multiple scattering paths to the intensity of the peak at 4 Å. The fit was calculated over the range $1.0 \leqslant r \leqslant 4.1$ Å, including both the first and the second peaks.

$0.3 \lesssim x_{\text{guess}} \lesssim 0.95$, the final fitted value always converges to 0.95 within ± 0.06. For x outside of this interval the fitting program finds a local minimum away from the correct value. The fit is also sensitive to the range of the Fourier transform, the weighting scheme, even the window function used and the widths of the interval over which it was applied.

The multiple scattering contribution in EXAFS for the rotational and buckling defects (discussed previously) can be implemented in the fitting for estimation of the rotational or buckling angles. This effect has been previously used by Frenkel *et al.*[30] for determination of buckling angles of disordered mixed salts. The approach is to use the dependence of the scattering amplitude on the buckling angle, which can be approximated as a quadratic function of the angle, and to do quadratic interpolation using the most important double and triple scattering paths from noncollinear paths.[29,30] The quadratic interpolation consists of generation of a basis of such double and triple scattering paths at three different buckling angles by running FEFF on such configurations. These paths are weighted in a constrained fit involving the angle to be determined as a fitting parameter. This can be accomplished by directly using the Lagrange's interpolating polynomial of second degree.[31] The scattering phase shifts for the double and triple scattering paths affected by the buckled or rotated sites should also be affected by the noncollinearity of the paths, but the phase shifts in Fig. 8 [the (c)–(e) set of curves] show that this effect is very small since the increase of the concentration of rotations does not show a significant change of the phase shifts. This behavior of the phases was observed in our simulations for small angles ($<20°$).

As an example of the fitting procedure we consider the case of a buckling angle of 10° present for all *B* sites in *XY* planes. This case does not require us to determine local defect concentrations and focuses only on the buckling angle determination. The basis of double and triple scattering paths was calculated for buckling angles of 4°, 8°, and 15°. The rest of the paths used are single scattering paths. The $|\chi(r)|$ for the data and the fit in the r range $1.0 \leqslant r \leqslant 4.1$ Å are shown in Fig. 11. The fit was made with the k range $2.8 \leqslant k \leqslant 16.4$ Å^{-1}, k^2 weight, Hanning window with margins of 2 Å^{-1}. This gave 26 independent data points which were fitted with 5 variables. The initial value of the buckling angle in the fit was 7° and the value found in the fit was $10.03° \pm 2.75°$. For starting buckling angle values in the interval $5° \lesssim \theta \lesssim 13°$, the fitting always converged very close to 10° with an error of approximately $\pm 3°$. Outside of this interval the fitting program finds a local minimum and the angle is different from the correct value. Given the sensitivity of the fit to the input parameters, it is clearly an interesting problem to find a self-consistent way of making these multiparameter nonlinear least squares fits.

IV. SUMMARY AND CONCLUSIONS

We have studied the signatures of local octahedral static distortions (radial, buckling, or rotational) by simulations of configurationally averaged PDF's and EXAFS spectra on model three-dimensional binary structures.

The following major conclusions can be drawn.

(i) The availability of *both* structural probes (PDF and EXAFS) allowed us to effectively distinguish the radial from the buckling and rotational displacements and to determine that only one of the atomic types in the binary had static displacements. Clearly, the complementarity of the two probes indicates that they both should be used for determination of studied structures whenever possible.

(ii) We showed how the local displacements propagate in the PDF's and in the EXAFS real-space moduli and phase shifts for the most affected shells to give the qualitative characteristics for the various distortions. This is the information used to decide on a specific local distortion when experimental data is to be fitted with a specific model. The magnitude of the static distortion can be estimated from the first peak of

the correlation function defined through the absolute values of the differences of the PDF for the long-range structure and the measured PDF with local displacements present.

(iii) Once a proposed distortion is chosen, constrained fits of the EXAFS show that multishell contributions to a single unresolved peak give correct estimates of the atom populations of the different shells used in the fit.

(iv) Similar fits with constraints using the effect caused by the multiple scattering in the EXAFS allow small buckling angles ($<20°$) to be determined. However, one should be cautious with the multivariable fits in EXAFS, since small deviations in the input can easily lead to a local minimum in the nonlinear least squares fitting output. Clearly, much remains to be done to improve the self-consistency of such fitting procedures as well as implementation of better statistical methods for understanding of the fitting results.

The application of these ideas to the analysis of experimental data would improve the quantitative determination of different patterns of local structure. A subject of future work in this direction will be to study the distortions in materials with layer and chain anisotropies. Finally, the addition of dynamic lattice effects will allow systematic understanding of these structures on different time and space scales and their interrelationships.

ACKNOWLEDGMENTS

D.A.D. thankfully acknowledges very stimulating discussions with S. J. Billinge, C. H. Booth, T. Egami, G. H. Kwei, D. Louca, M. Newville, and H. Röder. Work at the Los Alamos National Lab was supported by the U. S. Department of Energy.

[1] P. A. Lee, P. H. Citrin, P. Eisenberger, and B. M. Kincaid, Rev. Mod. Phys. **53**, 769 (1981); *X-Ray Absorption, Principles, Applications, Techniques of EXAFS, SEXAFS and XANES*, edited by D. C. Konigsberger and R. Prins (Wiley, New York, 1988).

[2] T. Egami, Mater. Trans., JIM **31**, 163 (1990).

[3] B. H. Toby and T. Egami, Acta Crystallogr., Sect. A: Found. Crystallogr. **48**, 336 (1991).

[4] Extended list of references to EXAFS and PDF measurements of lattice distortions in high-temperature superconductors can be found, e.g., in *Lattice Effects in High-T_c Superconductors*, edited by Y. Bar-Yam, T. Egami, J. Mustre de Leon, and A. R. Bishop (World Scientific, Singapore, 1992); T. Egami and S. J. L. Billinge, Prog. Mater. Sci. **38**, 359 (1994); T. Egami and S. J. L. Billinge, in *Physical Properties of High Temperature Superconductors V*, edited by D. M. Ginsberg (World Scientific, Singapore, 1996), p. 265.

[5] T. A. Tyson, J. Mustre de Leon, S. D. Conradson, A. R. Bishop, J. J. Neumeier, H. Röder, and Jun Zang, Phys. Rev. B **53**, 13 985 (1996); C. H. Booth, F. Bridges, G. J. Snyder, and T. H. Geballe, *ibid.* **54**, R15 606 (1996).

[6] C. H. Booth, F. Bridges, G. H. Kwei, J. M. Lawrence, A. L. Cornelius, and J. J. Neumeier, Phys. Rev. Lett. **80**, 853 (1998); C. H. Booth, F. Bridges, G. H. Kwei, J. M. Lawrence, A. L. Cornelius, and J. J. Neumeier, Phys. Rev. B **57**, 10 440 (1998).

[7] S. J. Billinge, R. G. DiFrancesco, G. H. Kwei, J. J. Neumeier, and J. D. Thompson, Phys. Rev. Lett. **77**, 715 (1996).

[8] D. Louca, T. Egami, E. L. Brosha, H. Röder, and A. R. Bishop, Phys. Rev. B **56**, R8475 (1997); D. Louca, G. H. Kwei, and J. F. Mitchel (unpublished).

[9] J. C. Mikkelsen, Jr. and J. B. Boyce, Phys. Rev. Lett. **49**, 1412 (1982); J. C. Mikkelsen, Jr. and J. B. Boyce, Phys. Rev. B **28**, 7130 (1983); J. C. Woicik *et al.*, Phys. Rev. Lett. **22**, 5026 (1997); L. E. Cox, R. Martinez, J. H. Nickel, S. D. Conradson, and P. G. Allen, Phys. Rev. B **51**, 751 (1995); T. A. Tyson, S. D. Conradson, R. F. C. Farrow, and B. A. Jones, *ibid.* **54**, R3702 (1996).

[10] N. Sircon, B. Ravel, Y. Yacoby, E. A. Stern, F. Dogan, and J. J. Rehr, Phys. Rev. B **50**, 13 168 (1994).

[11] B. H. Toby, T. Egami, J. D. Jorgensen, and M. A. Subramanian, Phys. Rev. Lett. **64**, 2414 (1990).

[12] S. J. L. Billinge, G. H. Kwei, and H. Takagi, Phys. Rev. Lett. **72**, 2282 (1994).

[13] A. Bianconi and M. Missori, J. Phys. I **4**, 361 (1994); A. Bianconi, Solid State Commun. **89**, 933 (1994); A. Bianconi, N. L. Saini, A. Lanzara, M. Missori, T. Rossetti, H. Oyanagi, H. Yamaguchi, K. Oka, and T. Ito, Phys. Rev. Lett. **76**, 3412 (1996); A. Bianconi, M. Lusignoli, N. L. Saini, P. Bordet, Å Kvick, and P. G. Radaelli, Phys. Rev. B **54**, 4310 (1996); A. Bianconi, N. L. Saini, T. Rossetti, A. Lanzara, A. Perali, M. Missori, H. Oyanagi, H. Yamaguchi, Y. Nishihara, and D. H. Ha, *ibid.* **54**, 12 018 (1996); A. Lanzara, N. L. Saini, A. Bianconi, J. L. Hazemann, Y. Soldo, F. C. Chou, and D. C. Johnson, *ibid.* **55**, 9120 (1997).

[14] See, for example, *Fundamentals of Crystallography*, edited by C. Giancovazzo (Oxford University Press, New York, 1992), Chap. 2.

[15] D. A. Dimitrov, A. R. Bishop, and S. D. Conradson, Phys. Rev. B **56**, 2969 (1997).

[16] B. E. Warren, *X-ray Diffraction* (Dover, New York, 1990).

[17] For a short review of colossal magnetoresistance see, e.g., A. R. Bishop and H. Röder, Curr. Opin. Solid State Mater. Sci. **2**, 244 (1997).

[18] A. J. Millis, P. B. Littlewood, and B. I. Shairman, Phys. Rev. Lett. **74**, 5144 (1995); A. J. Millis, B. I. Shraiman, and R. Mueller, *ibid.* **77**, 175 (1996).

[19] H. Röder, Jun Zang, and A. R. Bishop, Phys. Rev. Lett. **76**, 1356 (1996).

[20] J. F. Mitchell, D. N. Argyriou, C. D. Potter, D. G. Hinks, J. D. Jorgensen, and S. D. Bader, Phys. Rev. B **54**, 6172 (1996).

[21] See, e.g., D. C. Rapaport, *The Art of Molecular Dynamics Simulations* (Cambridge University Press, Cambridge, 1995), pp. 85–90.

[22] B. K. Teo, *EXAFS: Basic Principles and Data Analysis* (Springer-Verlag, Berlin, 1986).

[23] E. D. Crozier, J. J. Rehr, and R. Ingalls, in *X-Ray Absorption, Principles, Applications, Techniques of EXAFS, SEXAFS and XANES* (Ref. 1), pp. 373–442.

[24] J. J. Rehr, R. C. Albers, and S. I. Zabinsky, Phys. Rev. Lett. **69**, 3397 (1992); A. L. Ankudinov, and J. J. Rehr, Phys. Rev. B **56**, R1712 (1997).

[25] S. I. Zabinsky, J. J. Rehr, A. Ankudinov, R. C. Albers, and M. J. Eller, Phys. Rev. B **52**, 2995 (1995).
[26] P. Villella (private communication); F. J. Espinosa *et al.* (unpublished).
[27] P. A. Lee and J. B. Pendry, Phys. Rev. B **11**, 2795 (1975).
[28] E. A. Stern, M. Newville, B. Ravel, Y. Yacoby, and D. Haskel, Physica B **208&209**, 117 (1995).
[29] M. Newville, FEFFIT program manual (unpublished).
[30] A. Frenkel, E. A. Stern, A. Voronel, M. Qian, and M. Newville, Phys. Rev. B **49**, 11 662 (1994).
[31] See, e.g., W. H. Press, B. P. Flannery, S. A. Teukolsky, and W. T. Vetterling, *Numerical Recipes* (Cambridge University Press, Cambridge, 1986).